

Published in final edited form as:

Biochemistry. 2013 December 3; 52(48): 8708–8721. doi:10.1021/bi4011573.

## The Sensitive Balance Between the Fully Folded and Locally Unfolded Conformations of a Model Peroxiredoxin†

Arden Perkins<sup>a</sup>, Kimberly J. Nelson<sup>b</sup>, Jared R. Williams<sup>a</sup>, Derek Parsonage<sup>b</sup>, Leslie B. Poole<sup>b</sup>, and P. Andrew Karplus<sup>a,\*</sup>

<sup>a</sup>Department of Biochemistry and Biophysics, Oregon State University, Corvallis, Oregon 97333

<sup>b</sup>Department of Biochemistry, Wake Forest School of Medicine, Winston-Salem, North Carolina 27157

### Abstract

To reduce peroxides, peroxiredoxins (Prx) require a key ‘peroxidatic’ cysteine, that in a substrate-ready fully folded (FF) conformation becomes oxidized to sulfenic acid, and then after a local unfolding (LU) of the active site, forms a disulfide bond with a second ‘resolving’ Cys. For *Salmonella typhimurium* alkyl hydroperoxide reductase C (*StAhpC*) and some other Prxs, the FF structure is only known for a peroxidatic Cys→Ser variant, which may not accurately represent the wild type enzyme. Here, we obtain the structure of authentic reduced wild type *StAhpC* by dithiothreitol treatment of disulfide form crystals that fortuitously accommodate both the LU and FF conformations. The unique environment of one molecule in the crystal reveals a thermodynamic linkage between the folding of the active site loop and C-terminal regions, and comparisons with the Ser-variant show structural and mobility differences from which we infer that the Cys→Ser mutation stabilizes the FF active site. A structure for the C165A variant (a resolving Cys to Ala mutant) in the same crystal form reveals that this mutation destabilizes the folding of the C-terminal region. These structures prove that subtle modifications to Prx structures can substantially influence enzymatic properties. We also present a simple thermodynamic framework for understanding the various mixtures of FF and LU conformations seen in these structures. Based on this framework, we rationalize how physiologically-relevant regulatory posttranslational modifications may modulate activity and propose a non-conventional strategy for designing selective Prx inhibitors.

### Introduction

Peroxiredoxins (Prx) are a ubiquitous family of enzymes which reduce peroxides and peroxynitrites via a reactive cysteine.<sup>1</sup> Members of the widespread PrxI subfamily, mostly found to form doughnut-shaped decamers, are thought to be responsible for reducing over

†This study was supported in part by National Institutes of Health grant RO1 GM050389 to L.B.P. and P.A.K.

\*To whom correspondence should be addressed: ph. 541-737-3200, fax: 541-737-0481, karplus@science.oregonstate.edu.

Supporting Information: Mass spectrometric data of wild type *StAhpC* crystals showing the shift from dimer to monomer when soaked with DTT (Figure S1). Mass spectrometric and crystallographic characterization of the C165A mutant crystals (Figure S2). Uninterpreted ligand density at the decamer-building interfaces (Figure S3). This material is available free of charge via the Internet at <http://pubs.acs.org>.

<sup>1</sup>Abbreviations: Prx - peroxiredoxin, *StAhpC* - *Salmonella typhimurium* alkyl hydroperoxide reductase component C, FF - fully folded, LU - locally unfolded, Cp - peroxidatic cysteine, Cr - resolving cysteine, LU<sub>S-S</sub> - locally unfolded disulfide form, LU<sub>SH</sub> - locally unfolded thiol form, LU<sub>C-term</sub> - C-terminally unfolded form, WT<sub>DTT</sub> - DTT-treated wild type structure, C165A<sub>DTT</sub> - DTT-treated C165A structure, FF<sub>WT</sub> - fully folded wild type, FF<sub>C46S</sub> - fully folded C46S mutant, *HsPrxIV* - *Homo sapiens* PrxIV, *HsPrxI* - *Homo sapiens* PrxI, *HsPrxV* - *Homo sapiens* PrxV, *ApTpx* - *Aeropyrum pernix* thiol peroxidase, PDB - Protein Data Bank, DTT - 1,4-dithiothreitol, BME - β-mercaptoethanol, MES - 2-(N-morpholino)ethanesulfonic acid, PBS - phosphate buffered saline, ALS - Advanced Light Source, NCS - non-crystallographic symmetry, TLS - translation libration screw, AML - artificial mother liquor.

90% of cytosolic and mitochondrial peroxides.<sup>1,2,3</sup> The study of Prx1 enzymes also has implications for antibiotic drug designs as knock-out strains of certain microbial pathogens show them to be important for surviving peroxynitrite exposure<sup>4</sup> (such as is generated by the host immune system<sup>5</sup>), for scavenging peroxide,<sup>6</sup> for colonization,<sup>7</sup> or even growth at oxygen levels at or above 4%.<sup>8,9</sup> Additionally, controlled inactivation of some eukaryotic Prx1 subfamily members by a peroxide-driven hyperoxidation of the reactive Cys to a Cys-sulfinate was proposed to play a role in allowing peroxide-mediated signaling.<sup>10</sup> The downstream oxidation of target proteins by locally accumulated hydrogen peroxide is increasingly recognized as important in many such signaling pathways<sup>11</sup> with particularly well-studied examples being the inhibition of protein tyrosine phosphatases via oxidation of an active site cysteine.<sup>11,12,13,14,15</sup> Physiologically relevant regulation of Prx1 enzymes is also thought to occur by phosphorylation,<sup>11, 13,16,17</sup> lysine acetylation,<sup>18</sup> glutathionylation,<sup>19</sup> and proteolysis.<sup>11,20</sup>

Structural studies have shed much light on the mechanism of the Prx1 family of Prx enzymes (also called typical 2-Cys Prxs). For these enzymes, key residues are a peroxidatic Cys, termed C<sub>P</sub>, contained within an absolutely conserved PXXX(T/S)XXC motif, an additional conserved Arg, and a resolving Cys, termed C<sub>R</sub>, located near the C-terminus<sup>1,21</sup> (Fig. 1a). The basic active unit involves a so-called “B-type” homodimer with two active sites, each involving the C<sub>P</sub> from one subunit and C<sub>R</sub> from the other (Fig 1a), with the association of five such dimers at “A-type” interfaces building the toroidal (α<sub>2</sub>)<sub>5</sub> decamer (Fig 1b).<sup>22</sup> The active site stabilizes the C<sub>P</sub> thiolate (pK<sub>a</sub> ~6.0),<sup>23</sup> as well as specifically binding and activating the peroxide substrate.<sup>1,24</sup> In the catalytic cycle (Fig. 1c), an S<sub>N</sub>2 nucleophilic attack of the C<sub>P</sub> thiolate on the peroxide substrate forms a C<sub>P</sub>-sulfenic acid and water (or corresponding alcohol); the C<sub>P</sub>-sulfenic acid is then attacked by C<sub>R</sub> to form an interchain C<sub>P</sub>—C<sub>R</sub> disulfide (and another molecule of water) which is in turn reduced most commonly by a thioredoxin-type protein.<sup>1,21,24</sup>

In the enzyme form that reacts with peroxide, C<sub>P</sub> and C<sub>R</sub> are ~14 Å apart and C<sub>R</sub> is buried, so that formation of the C<sub>P</sub>—C<sub>R</sub> disulfide requires a substantial local unfolding of both the active site loop (i.e. residues ~40-50 which contains C<sub>P</sub>) of one chain and the C-terminus (containing C<sub>R</sub>) of its partner chain in the homodimer. Each active site of these enzymes, therefore, has at least two discrete conformations relevant to the catalytic cycle (Fig 1): (1) a fully folded conformation (FF), with a substrate-ready active site pocket, and (2) a locally unfolded conformation (LU) having the active site loop rearranged and the C-terminal residues beyond C<sub>R</sub> disordered.<sup>1,25</sup> This FF↔LU transition is not only important for catalysis, but it has been shown to be the main factor governing the sensitivity of Prx1 subfamily enzymes to hyperoxidative inactivation.<sup>10</sup> Some remaining points of uncertainty are, however, to what extent the unfolding of the active site loop and C-terminus are coordinated, how the conformational equilibrium is altered by modifications, and whether the catalytic states of C<sub>P</sub>-SH and C<sub>P</sub>-SOH are locked into a certain conformation or dynamically transitioning between them. NMR and crystallographic evidences imply that there is a preexisting dynamic equilibrium for the C<sub>P</sub>-SH form for a monomeric plant enzyme in the PrxQ subfamily,<sup>25,26</sup> while one human Prx1 subfamily enzyme has recently been reported to specifically convert to the LU conformation when in the C<sub>P</sub>-SOH form.<sup>27</sup>

We address these questions here using *Salmonella typhimurium* alkyl hydroperoxide reductase C (*StAhpC*), one of the first discovered Prxs and a model system for studying Prx1 catalysis,<sup>28, 29</sup> oligomerization,<sup>22</sup> and regulation.<sup>10</sup> Among the six *StAhpC* crystal structures reported, four exhibit the LU disulfide conformation (LU<sub>S-S</sub>) – with one wild type<sup>22</sup> and four mutants<sup>29,23</sup> – while only one, a C<sub>P</sub>→Ser (i.e. C46S) mutant, adopts the FF conformation.<sup>10</sup> We speculated that the *StAhpC* C46S mutant structure may not accurately represent the properties of the reduced wild type enzyme, and thus sought to obtain a

structure of the authentic wild-type FF active site. Here, we report that soaking the LU<sub>S-S</sub> form crystals in dithiothreitol (DTT) provides a structure of FF wild-type *StAhpC* (FF<sub>WT</sub>) in a crystal environment that can accommodate both the FF and LU conformations. In addition, we developed a protocol to crystallize the C<sub>R</sub>→Ala mutant in the same crystal form. This allows for a rare level of insight into the conformational, dynamic, and thermodynamic aspects of the FF↔LU equilibrium that are essential for Prx function, including how they are influenced by C<sub>P</sub>→Ser and C<sub>R</sub>→Ala mutations.

## Experimental Procedures

### Crystallography

**C165A creation and purification of wild type and mutant AhpC proteins**—The C165A mutation of *StAhpC* was created using the QuikChange site-directed mutagenesis kit (Stratagene) and validated by sequencing the entire gene. Wild type and mutant *StAhpC* were expressed from the pTHCm-*ahpC* vector<sup>23</sup> in JW0598 (lacking *ahpC*) *E. coli* cells<sup>30</sup> grown in Studier's ZYM-5052 auto-induction media.<sup>31</sup> The purification procedure for all AhpC mutant proteins was essentially the same as described previously<sup>32</sup> except that 10 mM β-mercaptoethanol (BME) was included in all buffers used during the purification of C165A in order to prevent hyperoxidation of the C<sub>P</sub>. After purification by phenyl sepharose and ion exchange chromatography, the C165A protein was concentrated and exchanged into 25 mM potassium phosphate, pH 7.0, 1 mM EDTA, 2 mM DTT. As seen from the results, apparently some BME remained present after the buffer exchange. The concentration of AhpC was determined by absorbance at 280 nm with  $\epsilon = 24,300 \text{ M}^{-1} \text{ cm}^{-1}$ .<sup>32</sup>

**Crystallization of wild type *StAhpC* and C165A mutant**—Initial crystallization was essentially as described by Wood et al.<sup>22</sup> For wild type, optimal crystals were grown at 300 K in hanging drops formed by 4 μL of 14.3 mg/ml protein (in 25 mM phosphate-buffered saline (PBS), 1mM EDTA, pH 7.0) mixed with 1 μL of artificial mother liquor (AML) containing 1.4 M MgSO<sub>4</sub> and 0.1 M MES at pH 6.5. Micro-seeding produced larger and better-diffracting crystals. Briefly, initial crystals were crushed in 100 μL of AML and vortexed, and a serial dilution of seed stock concentrations was created. Drops were seeded by dipping a 21-gauge needle into the seed stock and then streaking it across the new drop. Large, tapering column crystals on the order of ~0.5 mm grew in 1-14 days. As expected, these crystals contained protein in the disulfide form, and for reduction, crystals were soaked for two minutes in freshly prepared AML containing 0.1 M DTT (Fig. S1). Some stress lines did appear on the crystals when this soak was performed.

Many attempts to grow C222<sub>1</sub> crystals of untreated C165A produced only a single crystal that grew after more than a month. Peroxide at 100 mM was added to some crystallization trials to attempt to produce homogeneous oxidized protein, and crystals grew much more readily. Analysis of the treated protein by mass spectrometry showed that the predominant redox states of the enzyme were C<sub>P</sub>-SO<sub>3</sub><sup>-</sup> and a form with the molecular weight expected for a BME adduct that presumably was produced by residual BME from the purification reacting with transiently formed C<sub>P</sub>-SOH (Fig. S2). These crystals yielded a structure that was 100% LU but when soaked with DTT a portion of the enzyme shifted to the FF conformation. We inferred that the portion of the protein forming the BME-adduct was being reduced and shifting its conformation to FF, and the portion containing C<sub>P</sub>-SO<sub>3</sub><sup>-</sup> was not being reduced and was remaining in the LU conformation. Though not conclusive, this observations implies that the C<sub>P</sub>-SO<sub>3</sub><sup>-</sup> form of *StAhpC* behaves differently than two other Prxs for which this form was shown to be FF.<sup>33,34</sup> In refining the protocol to produce maximal C165A-BME adduct with minimal C<sub>P</sub>-SO<sub>2</sub><sup>-</sup>/SO<sub>3</sub><sup>-</sup> formation, we settled on the addition of 10 μM BME and 20 μM peroxide based on trials of several concentrations that

were analyzed with mass spectrometry (Fig S2). In our final protocol, crystals of C165A were obtained by seeding with crushed wild type LU<sub>S-S</sub> crystals in drops first treated with 10  $\mu$ M BME for 30 minutes, with the subsequent addition of hydrogen peroxide to a final concentration of 20  $\mu$ M. A DTT soak of these crystals was carried out as for wild type *StAhpC*. Here, we refer to the DTT-soaked structures of wild type and C165A as WT<sub>DTT</sub> and C165A<sub>DTT</sub>, respectively.

For freezing both wild type and C165A crystals, glycerol was added to the drop as a cryoprotectant to make a final concentration of  $\sim$ 20%. The crystals dissolved if the glycerol was added too quickly, so the glycerol was placed beside the crystal drop and a small channel was created between them with a pipette tip and equilibrated for  $\sim$ 2 min. The crystals were then scooped and frozen by plunging into liquid nitrogen.

**Data collection**—Data were collected at the Advanced Light Source (ALS) Lawrence Berkeley National Laboratory beam-lines 5.0.2. and 8.2.2. The data were indexed and integrated with Mosflm version 7.0.9.<sup>35</sup> All crystals of *StAhpC* were found to be in the space group C222<sub>1</sub> and exhibited similar unit cell dimensions as previous *StAhpC* structures, with  $a \sim 127$  Å,  $b \sim 171$  Å,  $c \sim 135$  Å (see Table 1). The resolution cutoff criterion was based on the new statistic  $CC_{1/2}$  recently introduced by Karplus and Diederichs,<sup>36</sup> which demonstrated that better models are obtained when resolution is extended to the  $CC_{1/2} = 0.1$ -0.2 range despite the fact that  $R_{meas}$  values become disturbingly large and  $\langle I/\sigma \rangle$  unconventionally low. We have applied this new criteria in recent studies and discussed its value,<sup>25,37</sup> and note a recent detailed study by Evans & Murshudov<sup>38</sup> concluded that useful signal is contained in data out to the  $CC_{1/2} \sim 0.2$ -4 range and “it seems sensible to set a generous limit so as not to exclude data containing real (if weak) information.” For our structures, we implemented a cutoff of  $CC_{1/2} \sim 0.2$  in the highest resolution shell (Table 1) and obtained improved maps. The effective resolution of a structure is difficult to define, but for comparison with past structures, we also note the resolution at which  $\langle I/\sigma \rangle \sim 2$  (Table 1).  $R_{free}$  flags were randomly assigned to five percent of the WT<sub>DTT</sub> dataset, and the same flags were imported to use for the C165A<sub>DTT</sub> dataset.

**Refinement of DTT-soaked structures**—An initial model for WT<sub>DTT</sub> was constructed based on the *StAhpC* C46S crystal structure (PDB entry 1n8j of spacegroup P<sub>1</sub>)<sup>10</sup> with active site residues 40-50 and 161-186 removed to produce maps that were unbiased for these regions. Chains K, L, O, P, and R of 1n8j were superimposed on the half-decamer of PDB entry 1yep, one of the previously solved locally-unfolded C222<sub>1</sub> *StAhpC* structures,<sup>22</sup> and this model was refined using BUSTER,<sup>39</sup> producing initial  $R/R_{free}$  values of 25.0/28.9. All chains were found to have had their disulfides reduced, and the active sites were modeled as FF or LU<sub>SH</sub> (LU with no disulfide formed) or LU<sub>C-term</sub> (only the C-terminal region unfolded), based on omit map density (Table 2). Coot<sup>40</sup> was used to perform manual rebuilding, with main initial changes including the addition of solvent molecules and adjustment of some side-chain rotamers. No non-crystallographic-symmetry (NCS) restraints were used. End stage refinements were performed with PHENIX.<sup>41</sup> Adding riding hydrogens reduced  $R_{free}$  by  $\sim$ 0.5 percent, and using TLS refinement with one group per protein chain, dropped  $R_{free}$  by  $\sim$ 3 percent. The occupancy of the chain B active site loop was estimated to be  $\sim$ 0.5:0.5 FF:LU. We expect that remaining positive difference density in this region is due to solvent molecules that coordinate with Arg119 when the active site is LU, as was observed in the LU<sub>S-S</sub> structure.<sup>22</sup> Based on evidence (see Fig. 2 legend), residual positive difference map peaks at sites that had been modeled as waters were replaced by potassium and chloride ions and six glycerol molecules. There remains one fairly large and oddly-shaped difference density feature at each decamer-building interface, which we were not able to interpret (Fig. S3). The WT<sub>DTT</sub> final  $R/R_{free}$  was 20.4%/24.0%, and the final refinement statistics are reported in Table 1.

Refinement for C165A<sub>DTT</sub> utilized the final WT<sub>DTT</sub> model as a starting model with active site residues 40-50 and 160-186 removed (initial R/R<sub>free</sub> = 24.4/26.4). As for WT<sub>DTT</sub>, the chain B active site loop was modeled as 50:50 LU<sub>SH</sub>/LU<sub>C-term</sub>. Residues 40-50 of chains A, C, D, and E were modeled only as fully-occupied FF despite residual low level density that could be due to some LU population; the C-terminal regions were modeled as partially occupied FF based on consistent 2F<sub>O</sub>-F<sub>C</sub> and F<sub>O</sub>-F<sub>C</sub> density for the expected FF chain path. Test refinements varying the occupancy in increments of 0.1 gave 0.6 as the occupancy at which the B-factors for this region were closest to those observed for the WT<sub>DTT</sub> structure. A residual difference peak near the position occupied by wild type Cys165-S $\gamma$  was left uninterpreted, and we suspect it is due to a partially-occupied sulfhydryl from DTT (present at ~0.1 M) that binds at this site when the C-terminus is not folded. Both mass spectrometry on these crystals (Fig. S2), and reasonably clear electron density for Ala165 in chain A confirm the crystals are of the C165A mutant. Using the reference restraint option of Phenix<sup>41</sup> the WT<sub>DTT</sub> structure was utilized to restrain the geometries of the weakly-occupied C-terminal regions. Riding hydrogens were added to the model and one TLS group per chain was implemented to reach final R/R<sub>free</sub> values of 19.9/23.9 (Table 1). The coordinates and structure factors for the WT<sub>DTT</sub> and C165A<sub>DTT</sub> structures have been deposited in the Protein Data Bank as PDB codes 4ma9 and 4mab.

### Mass spectrometry analysis

Crystal samples were prepared from crystals harvested into a 10  $\mu$ L drop of degassed DI water, manually crushed, and kept from further chemical reactions by flash-freezing in liquid nitrogen prior to analysis. Proteins were detected from 800-2000 m/z using a LTQ-FT Ultra mass spectrometer (Thermo, San Jose, CA, US) in LTQ mode, with a Finnigan Ion Max API source set up for electrospray ionization in positive ion mode. All collections used the following conditions: spray voltage 5 kV, capillary temperature 200 $^{\circ}$  C, capillary voltage 40 V, and tube lens 240 V. Proteins from samples described above were adsorbed onto a C4 Ziptip, washed with water and eluted in-line to the mass spectrometer with solvent as previously described.<sup>42,43</sup> The solvent of 50% acetonitrile, 50% water and 0.1% formic acid was delivered at 20  $\mu$ L/min. Maximum entropy deconvolution and integration of the mass spectrum was performed to generate zero charge parent masses from the mass spectra using the program MOP (Multiple Overlaying Pictures, Spectrum Square Associates, Inc) and Matlab.<sup>42</sup> Spectra of crystals were noisy, but clearly showed that WT<sub>DTT</sub> was predominantly monomeric (indicating reduction of the intermolecular disulfide, Fig. S1) and C165A<sub>DTT</sub> was mostly in the thiol/thiolate state, though there were minor peaks near the expected positions of C<sub>P</sub>-SOH, C<sub>P</sub>-SO<sub>2</sub><sup>-</sup>, and C<sub>P</sub>-SO<sub>3</sub><sup>-</sup> (Fig. S2). The time course assay for C165A was performed on reduced protein at 43.5  $\mu$ M in 100-fold diluted PBS buffer,<sup>44</sup> pH 7.0, with the addition of peroxide to make the final concentration 1 mM. Samples were taken at 0, 1, 2, 3, 5, 10 and 20 minutes and analyzed as specified above.

## Results and Discussion

### Overall structure

Recognizing that the existing *StAhpC* wild type LU<sub>S-S</sub> structure<sup>22</sup> had few crystal contacts involving residues that change positions in the FF $\leftrightarrow$ LU transition (Fig 1b), we conceived of generating the FF conformation by soaking the LU<sub>S-S</sub> crystals in DTT. Fresh crystals of the disulfide form of wild type *StAhpC*<sup>22</sup> survived the DTT soak with diffraction power and unit cell virtually unchanged, allowing the structure to be determined at 1.82  $\text{\AA}$  resolution using recently proposed<sup>36</sup> more generous resolution cutoff criteria (Table 1). We identified bound potassium and chloride ions (Fig. 2), which may relate to how ionic strength can increase decamerization, FF stability, and catalytic activity,<sup>29</sup> as has been reported for another AhpC.<sup>45</sup> In this crystal form a half-decamer of five chains (labeled A-E) are in the

asymmetric unit, with the AB, CD, and  $EE_{\text{sym}}$  (symmetry mate of E) pairs being the functional homodimer units (Fig. 1b).<sup>22,29</sup> For the wild-type DTT-treated structure ( $WT_{\text{DTT}}$ ), disulfide reduction did occur, as the active site loop (residues 40-50) for chains A, C, D, E, and the C-termini of their partner chains (B, D, C, and  $E_{\text{sym}}$ , respectively) adopt the FF conformation, and the  $C_P$  and  $C_R$  thiulates/thiols are visible in their expected positions  $\sim 14$  Å apart (Fig. 3a,b). Mass spectrometry of dissolved  $WT_{\text{DTT}}$  crystals confirmed the presence of the reduced monomeric form (Fig. S1). Interestingly, the active site loop of chain B exhibits a  $\sim 50:50$  mix of the FF/LU chain paths (Fig. 3c), and its partner in the dimer, chain A, has its C-terminus LU (only modeled through residue 163) even though no  $C_P$ — $C_R$  disulfide is present (Fig. 1a). This C-terminal LU conformation can be explained in that a crystal packing interaction blocks the position it would fill in the FF conformation (Fig. 1b).

Thus, in this crystal, three new conformations containing reduced  $C_P$  and  $C_R$  residues are observed (Table 2). One, as targeted, is the FF conformation adopted by the wild type enzyme that is seen four times in the asymmetric unit and which we refer to as “ $FF_{\text{WT}}$ ” (Fig. 3a and 3b). The others are both  $\sim 50\%$  occupied and pair an LU C-terminus with either an LU active site loop without a disulfide (“ $LU_{\text{SH}}$ ”), or with an FF active site loop (“ $LU_{\text{C-term}}$ ”) (Fig. 3c). For clarity, since each complete active site combines residues from two chains, we will use here a nomenclature that first defines the chain contributing  $C_P$  and then the chain contributing  $C_R$ , and using a prime (') to denote residues from the chain contributing  $C_R$ . Thus, the four  $\sim 100\%$   $FF_{\text{WT}}$  active sites are the  $AB'$ ,  $CD'$ ,  $DC'$ ,  $EE'_{\text{sym}}$  active sites, and the 50:50 mix of the  $LU_{\text{SH}}$  and  $LU_{\text{C-term}}$  conformations occurs in the  $BA'$  active site. An advantage of this crystal form is it provides a controlled environment in which *StAhpC* structures are each seen in two basic contexts — one with unconstrained C-termini and active site loop regions (active sites  $AB'$ ,  $CD'$ ,  $DC'$ , and  $EE'_{\text{sym}}$ ) and one with a C-terminus constrained to be unfolded and unconstrained active site loop (active site  $BA'$ ). A summary of the conformations seen in *StAhpC* structures compared in this paper are given in Table 2.

### Linkage of the active site loop and C-terminal conformations

#### Asymmetry of interactions linking the C-terminal and active site loop regions

—As noted above, for the  $BA'$  active site, the A-chain C-terminal region is blocked from adopting the FF conformation by a crystal contact. Our observance of the  $LU_{\text{C-term}}$  conformation in this active site proves that the active site loop can be FF even when the C-terminal region is LU. In addition, because the  $BA'$  active site loop was  $\sim 50\%$  LU (as opposed to dominantly FF as for the other active sites) implies a thermodynamic linkage in which the absence of a folded C-terminal region destabilizes the FF active site loop.

Comparing the  $FF_{\text{WT}}$  and  $LU_{\text{SH}}$  structures in the region of the active site (Fig. 4a) shows that unfolding of the C-terminus could destabilize the active site loop in three ways. First is the loss of hydrophobic packing interactions between Leu176', Leu182', and Ile186' side chains and the first turn of helix  $\alpha_2$ . Second is a less direct effect mediated by residues 137-142 which in the FF conformation make a short  $\beta$ -sheet with C-terminal residues 163'-166' (Fig. 4a). When 163'-166' move away in the LU transition, the 137-142 segment shifts  $\sim 1.5$  Å, pulling with it Glu49 which is H-bonded with 142-NH (Fig. 5). This shifting of the Glu49 and Glu138 carboxylates contribute to a disordering of Arg119 and the weakening of its interactions with the FF  $C_P$  side chain (Fig. 5). Third, a contribution not relevant for the crystalline decamer but expected to occur in solution, is that the loss of the packing from the side chains of Leu180' and Val183' with a hydrophobic niche (residues 15-20) at the decamer-building interface (Fig. 4a) would destabilize the decamer and therefore, as has been noted before,<sup>22</sup> destabilize the active site loop.

In these ways, unfolding of the C-terminus destabilizes the FF active site loop, but does not force its unfolding. In contrast, the unfolding of the active site loop will not just destabilize the C-terminal segment, but will actually *force* it to unfold (Fig. 4b). This asymmetric linkage occurs because the LU positions of the active site loop backbone physically collide with the FF positions of Leu176', Leu182', and Ile186'.

**Active site loop and C-terminal region B-factor patterns provide additional evidence of linkage**—For the AB', CD', DC', and EE'<sub>sym</sub> active sites in this crystal form, both LU<sub>S-S</sub> (as grown) and FF (after reduction by DTT) conformations can be adopted, proving that the mobility of these active sites are not hindered by the crystal packing. Therefore, additional evidence of a physical linkage between the active site loop and C-terminal conformations can be gleaned from their B-factors, which show that a correlation exists between their dynamic properties, with more ordered active site loops (lower B-factors) paired with more ordered C-termini (Fig. 6 inset). The detailed B-factor patterns of the chains, controlled for the crystal environment, further illustrates this linkage. Interestingly, all five regions associated with the FF↔LU transition are the high B-factor peaks, and of these regions three – the active site loop, the C-terminus, and residues 85-87 which H-bond to the Ile186' α-carboxylate – become even more disordered in the transition from FF<sub>WT</sub> to LU<sub>S-S</sub> (black vs. green curves in Fig. 6). That all five segments are rather mobile in both FF<sub>WT</sub> and LU<sub>S-S</sub> leads us to conclude that they are easily adaptable rather than being highly stabilized in either conformation, and this helps keep the energy barrier to the conformation change low.

### Changes associated with the C<sub>P</sub>→Ser mutation

**Positional differences in the FF active site**—In addition to *StAhpC*, many structures of FF Prx enzymes have only been solved as C<sub>P</sub>→Ser mutants<sup>46,47,48,49,50,51,52,53</sup> assuming that a serine in the reactive C<sub>P</sub> position faithfully mimics the active site. Given that an active site Cys→Ser mutation can alter the thermodynamics of a folded protein sufficiently to cause substantial rearrangement of the active site,<sup>54,55</sup> we looked for differences caused by the C46S mutation by comparing the 4 FF<sub>WT</sub> active sites with the 20 independent FF active sites seen in crystals of the C46S mutant (FF<sub>C46S</sub>)<sup>10</sup> (Fig. 7a). Although the FF<sub>WT</sub> and FF<sub>C46S</sub> structures are very similar (rmsd ~0.35 Å for 186 C<sub>α</sub>-atoms), the sets of FF<sub>WT</sub> and FF<sub>C46S</sub> structures cluster distinctly (Fig. 7a), revealing systematic active site differences. For clarity in this comparison, we refer to the C46S mutant structure as being “shifted” relative to the wild type.

Despite conservation of the C<sub>P</sub> backbone position, Ser46-O<sub>γ</sub> is shifted consistently by ~1 Å compared to Cys46-S<sub>γ</sub>, and is further from Ala40-NH, Thr43-O<sub>γ</sub>, and Arg119-NH2, and closer to Arg119-NH1 (Fig. 7a). Also, the side chains of Arg119 and Pro39 shift slightly and Thr43 sits deeper in the active site pocket. Independent evidence for which of these shifts are due to the Cys→Ser mutation can be gleaned from the prototypical Prx substrate-bound structures of *Aeropyrum pernix* thiol peroxidase (*ApTpx*, a Prx6 family member despite the “Tpx” name;<sup>1</sup> PDB code 3a2v)<sup>56</sup> (Fig. 3a) and the diol inhibitor-bound *Homo sapiens* PrxV (*HsPrxV*; PDB code 3mng),<sup>24</sup> which fortuitously have high resolution structures available for both the wild type and C<sub>P</sub>→Ser forms.<sup>1</sup> In both cases, similar shifts are seen for the Ser, Arg, and Thr side chains, and these structures additionally show that bound ligands sit deeper in the active site of the C<sub>P</sub>→Ser mutants (Fig. 7b and c).

In rationalizing these common shifts, we assume, for a few reasons, that the C<sub>P</sub> residue in the wild type structures is present as the catalytically relevant thiolate: first, the *StAhpC* crystals are grown at pH 6.5, above the experimentally measured C<sub>P</sub> pK<sub>a</sub> of 5.9 +/- 0.1;<sup>23</sup> second, the peroxide-bound *ApTpx* crystals (PDB code: 3a2v) were at pH 6.5 and

catalytically active;<sup>24</sup> third, all the *HsPrxV* structures, ranging from pH=5.6 to pH=8.0, adopt similar active site geometry;<sup>24</sup> and fourth, the interactions between S $\gamma$  and its active site surroundings are compatible with the thiolate interpretation (Fig. 7). It is to be expected that a hydroxyl would not be able to perfectly mimic a thiolate, as the thiolate is both larger (van der Waals radius  $\sim 0.7$  Å greater), cannot donate a hydrogen bond, and with its more diffuse electron clouds is “softer,” making for rather different H-bonding properties.<sup>57,58</sup> We attribute the Ser and Arg shifts to making the Arg119-NH1 $\cdots$ O $\gamma$  H-bond shorter and better aligned in the mutant, and the Thr shift as filling in the space opened by the S $\gamma$  to O $\gamma$  change while improving the linearity of its H-bond with the backbone carbonyl.<sup>59</sup> The  $\sim 0.5$  Å deeper penetration of ligands into the active sites of C<sub>P</sub>→Ser mutants (Fig. 7b and c) would be both due to the smaller van der Waals radius of oxygen and the formation of a Ser-O $\gamma$ H ... ligand H-bond. Given such structural differences it should not be surprising that the C46S mutation may also have thermodynamic consequences.

**B-factors and crystallizability indicate mutation-induced alterations to mobility**—Beyond the changes in atom positions, we also observed striking differences between the B-factors of FF<sub>WT</sub> and a FF<sub>C46S</sub> active site that is not constrained by crystal contacts (Fig. 6). Relative to their respective cores, FF<sub>C46S</sub> has B-factors about half as high as the FF<sub>WT</sub> in all three regions of the structure that change positions in the FF $\leftrightarrow$ LU transition (yellow highlights). This greater order of C46S provides evidence that in some way the C<sub>P</sub>-Ser mutation has a stabilizing effect on the FF active site, and we propose that this apparent stabilizing effect is at least in part due to the Ser-Arg hydrogen bond (Fig. 7a) being stronger than those formed by the sulfur atom.<sup>58</sup> The *ApTpx* and *HsPrxV* C<sub>P</sub>→Ser structures do not share this difference in B-factor patterns, but this may be due to a stabilizing effect of the bound inhibitors and/or crystal packing interactions.

Additional evidence for a difference in the dynamic properties of C46S and wild type *StAhpC* is that we were not able to crystallize the reduced wild type enzyme in the C46S mutant P<sub>1</sub> spacegroup,<sup>10</sup> despite the near identity of their average structures. The explanation we propose is that even though the FF conformation is dominant for the reduced wild type enzyme, LU or partially LU conformations are present at a high enough level to prevent growth of the P<sub>1</sub> crystals which have some packing interactions that are not compatible with the LU conformation. This is consistent with deuterium exchange analysis of reduced wild type *StAhpC* that revealed the active site loop as the least protected region.<sup>60</sup> These differences in *StAhpC* induced by the C<sub>P</sub>→Ser mutation reinforce two things: first, one must be cautious inferring the properties of the wild type enzyme from studies of such variants, and second, that the wild type active site has not evolved to be as highly stable as possible, as it would be counter-productive to catalysis (see also below).

### Structural characterization of the *StAhpC* C<sub>R</sub>→Ala mutant

Recently a study of *HsPrxIV* crystals that could accommodate both the FF and LU conformations showed that a resolving Cys→Ala mutant (*HsPrxIV*-C245A) adopted the FF conformation when reduced, but was LU after a 5 min 1 mM peroxide treatment said to generate the C<sub>P</sub>-SOH form.<sup>27</sup> Because of the apparent resistance of the C<sub>P</sub>-SOH to further oxidation, the authors concluded that once the newly-formed C<sub>P</sub>-SOH transitions to LU, “it does not reform the FF conformation until the peroxidatic cysteine is reduced.”<sup>27</sup> However, we note that a Western blot of similar treatments in that study showed an un-quantified portion of the sample was hyperoxidized to C<sub>P</sub>-SO<sub>2/3</sub>, and the identification of the C<sub>P</sub>-SOH state was only based on interpreting an electron density map that for some chains showed alternate conformations for the C<sub>P</sub> side chain. To address this important point further, we sought to use our *StAhpC* crystal form to crystallographically define thermodynamic impacts on the FF $\leftrightarrow$ LU equilibrium of both a C<sub>R</sub>→Ala mutation and C<sub>P</sub>-SOH formation.



**$\beta$ -mercaptoethanol (BME) as a crystallization aid**—We generated the equivalent *StAhpC* C<sub>R</sub>→Ala mutant (C165A), which as expected was active in the presence of a suitable reductant. As purified, the C165A variant did not readily crystallize, but crystal growth was strongly promoted by treatment with 100 mM hydrogen peroxide, and the resulting structure showed the protein in the LU conformation in what, based on the electron density, we originally modeled as the C<sub>P</sub>-SOH form (data not shown). However, mass spectrometric analyses of the crystals (Fig. S2) showed them to be a roughly 60:40 mix of a BME adduct (presumably a mixed disulfide with C<sub>P</sub>) and C<sub>P</sub>-SO<sub>3</sub> despite the lack of clear density for these modifications. Using this insight we created a C165A BME-adduct crystal by exposure to only  $\mu$ M levels of peroxide in the presence of added BME. We suggest based on this experience that, especially for C<sub>R</sub>-mutants or 1-Cys Prxs, trapping an otherwise dynamic Prx enzyme (e.g. <sup>26</sup>) in an LU, mixed-disulfide state (for instance, with BME) may enhance conformational homogeneity and serve as a generally useful crystallization aid.

**The structure of reduced C165A**—The BME-adduct crystal was soaked with DTT to yield a 1.9 Å resolution structure of reduced *StAhpC* C165A (Table 1; Fig. S2a). In this C165A<sub>DTT</sub> structure, the BA' active site (in which the C-terminal region cannot fold) is like WT<sub>DTT</sub> adopting a 50:50 mix of the LU<sub>SH</sub> and LU<sub>C-term</sub> conformations. However, for the other four active sites, the active site loops are visibly in the FF conformation with an unmodified C<sub>P</sub> side chain (Fig. S2b), but the C-termini have very weak electron density and were modeled at ~60% FF (Table 2). As little, if any, C<sub>P</sub> oxidation is present, the ~40% unfolding of the C-termini must reflect a destabilization caused by the C165A mutation itself. A mutation of a Cys→Ala in a buried, non-polar environment would be expected to be destabilizing.<sup>61</sup>

**Time course of C165A oxidation implies a dynamic C<sub>P</sub>-SOH form**—To seek conditions for generating pure C165A C<sub>P</sub>-SOH for crystallographic study, we used mass spectrometry to characterize its peroxide-driven C<sub>P</sub> oxidation. The time course reveals that S-BME and SOH forms appear early, and that as the BME is used up, the SOH peak smoothly decreases while the SO<sub>2</sub><sup>-</sup> peak increases (Fig. 8). This conversion implies that the *StAhpC* C<sub>P</sub>-SOH form is not locked into the LU conformation, but dynamically adopts the FF conformation from which it reacts with a second peroxide to form C<sub>P</sub>-SO<sub>2</sub><sup>-</sup>. Given this behavior, we were not able to create a pure C165A C<sub>P</sub>-SOH species for structural analysis.

The facile hyperoxidation of the *StAhpC* C165A variant is an expected result, and makes all the more surprising the report that *HsPrxIV*-C245A<sup>27</sup> resists hyperoxidation sufficiently to be crystallized as a stable C<sub>P</sub>-SOH form. Although the two proteins may behave this differently, another possibility is that despite the electron density map evidence, the peroxide-treated *HsPrxIV*-C245A structure was not C<sub>P</sub>-SOH, but a mixture of C<sub>P</sub>-SOH, C<sub>P</sub>-SO<sub>2</sub><sup>-</sup>, C<sub>P</sub>-SO<sub>3</sub><sup>-</sup> and/or mixed disulfide forms. Our experience noted above with the structure of C165A treated with 100 mM peroxide (where we had satisfactorily modeled C<sub>P</sub>-SOH into the electron density maps of protein that was mixture C<sub>P</sub>-SO<sub>3</sub><sup>-</sup> and a BME adduct) shows that electron density alone in an exposed region of a structure may be insufficient to differentiate between C<sub>P</sub>-SOH and higher oxidation states. While we agree that C<sub>P</sub>-SOH formation may indeed promote unfolding of the active site, we suggest that mass spectrometric characterization of the peroxide-treated *HsPrxIV*-C245A is needed before firm conclusions are drawn.

### A conceptual model for understanding the impact of Prx modifications on activity

The changes in conformation and equilibrium populations that we have observed highlight to what extent even slight modifications in or near the Prx active site can alter the enzyme's properties. Although the variety of effects appears complex, a simple thermodynamic model

for how the various modifications stabilize or destabilize the FF active site can account for the range of structural changes seen and help in understanding their implications for function (Fig. 9). The six curves illustrate how with changes in interaction energies of just a few kcal/mol, the FF $\leftrightarrow$ LU equilibrium can shift from 1000:1 to 1:100. The crystal structures analyzed here show a hierarchy of FF $\leftrightarrow$ LU equilibria (Table 2) that allow us to assign various *StAhpC* forms to the different curves (Fig. 9). Beginning with the most ordered FF active site, the *StAhpC* C46S mutant seems in the range of the orange to red curves (99.9 – 99% FF). The four FF<sub>WT</sub> active sites that are visibly FF (but less so than C46S) might be represented by the orange to yellow curves (99-90% FF), while the equivalent active sites in the C165A<sub>DTT</sub> structure — with the C-terminal region destabilized relative to wild type — would be between the yellow and green curves (90-50% FF). The BA' active site of the WT<sub>DTT</sub> structure with its ~50:50 mix of LU<sub>SH</sub>/LU<sub>C-term</sub> conformations is described by the green curve. Lastly, the BME adduct that strongly destabilizes the FF active site loop would be represented by the violet curve or above ( > 99% LU). Two key insights from these analyses are that (1) for wild type *StAhpC* the FF:LU free energy difference is not large, so even minor changes can substantially impact the enzyme's properties, and (2) given this sensitive positioning, the FF-stabilizing C<sub>P</sub>→Ser mutation and the FF-destabilizing C<sub>R</sub>→Ala mutation may each sufficiently perturb the FF $\leftrightarrow$ LU equilibrium that the measured properties of those mutants will not reliably report on the properties of the wild-type enzyme.

Though each Prx enzyme will have distinct properties, these concrete examples of the linkage between sequence, structure, and thermodynamics can be applied to understand the impact of how sequence variations and physiological Prx posttranslational modifications such as Thr/Ser phosphorylation and lysine acetylation, many of which occur in or affect the FF C-terminal region,<sup>10,11,13,16,17, 18,19</sup> may regulate both the enzyme's activity, and/or its sensitivity to hyperoxidation by altering the FF $\leftrightarrow$ LU equilibrium. Indeed, mutations disrupting in the C-terminal region of certain Prxs allowed them to retain activity and become much less sensitive to inactivating hyperoxidation.<sup>62,63</sup> Similarly, *in vivo* proteolytic C-terminal truncation<sup>20</sup> or the acetylation of *HsPrx1* at Lys197<sup>18</sup>, have both been reported to lower the enzyme's susceptibility to hyperoxidation, as would be expected if they destabilize the C-terminal packing.

### Targeting the prokaryotic Prx C-terminal region for drug design

Although it is most common to target the active sites of proteins for drug therapy, inhibitors that trap enzymes in conformations in which catalysis cannot occur offer an alternative strategy. A recent example is a small molecule inhibitor that holds a tumor-associated mutant of isocitrate dehydrogenase 1 in an open and un-reactive conformation.<sup>64</sup> As Prxs contain a universally conserved active site, yet exhibit highly divergent C-terminal regions, especially between human and prokaryotic homologs,<sup>1</sup> this latter strategy could be very useful for developing inhibitors selective for pathogen Prxs.<sup>10,44</sup> In particular, our observations here lead us to suggest three novel strategies for developing antibiotics that could diminish prokaryotic redox defenses through blocking Prx activity. First, molecules that disrupt the C-terminal packing (indicated by the upward arrow in Fig. 9) would decrease the amount of FF enzyme present and thus inhibit the enzyme's peroxidase activity. Second, and somewhat counter-intuitive, even more effective could be molecules capable of highly *stabilizing* the FF C-terminus of prokaryotic Prxs (indicated by the downward arrow in Fig. 9). These would strongly shift the equilibrium toward FF to promote (potentially to 100%) the hyperoxidation of C<sub>P</sub> so that inactive C<sub>P</sub>-SO<sub>2</sub>/3<sup>-</sup> states would accumulate. Third, in a special case that combines these effects, an inhibitor that both destabilized the FF active site and also blocked resolution of the C<sub>P</sub>-SOH state (similarly to the behavior of the *StAhpC*-C165A mutant) would both decrease peroxidase activity and promote formation of the

hyperoxidized forms. Because few prokaryotes possess a sulfiredoxin-type enzyme capable of reversing hyperoxidation of the peroxidatic cysteine,<sup>11</sup> the latter two approaches could be extremely effective, as the hyperoxidation to C<sub>P</sub>-SO<sub>2/3</sub><sup>-</sup> would cause permanent inactivation.<sup>65</sup>

## Supplementary Material

Refer to Web version on PubMed Central for supplementary material.

## Acknowledgments

The mass spectrometric analyses were enabled by the Oregon State University Environmental Health Science Center supported by NIEHS grant #P30 ES000210, and crystallographic data collection was done at the Advanced Light Source (ALS), supported by the Director, Office of Science, Office of Basic Energy Sciences, of the U.S. Department of Energy under Contract No. DE-AC02-05CH11231.

## References

- Hall A, Nelson K, Poole LB, Karplus PA. Structure-based Insights into the Catalytic Power and Conformational Dexterity of Peroxiredoxins. *Antioxid & Redox Signaling*. 2011; 15:795–815.
- Winterbourn CC. Reconciling the chemistry and biology of reactive oxygen species. *Nat Chem Biol*. 2008; 4:278–286. [PubMed: 18421291]
- Cox AG, Winterbourn CC, Hampton MB. Mitochondrial peroxiredoxin involvement in antioxidant defense and redox signaling. *Biochem J*. 2010; 425:313–325.
- Chen L, Xie Q, Nathan C. Alkyl Hydroperoxide Reductase Subunit C (AhpC) Protects Bacterial and Human Cells against Reactive Nitrogen Intermediates. *Mol Cell*. 1998; 1:795–805. [PubMed: 9660963]
- Fang FC. Perspectives series: host/pathogen interactions. Mechanisms of nitric oxide-related antimicrobial activity. *J Clin Invest*. 1997; 99:2818–2825. [PubMed: 9185502]
- Seaver LC, Imlay JA. Alkyl Hydroperoxide Reductase Is the Primary Scavenger of Endogenous Hydrogen Peroxide in *Escherichia coli*. *J Bacteriol*. 2001; 183:7173–7181. [PubMed: 11717276]
- Cosgrove K, et al. Catalase (KatA) and Alkyl Hydroperoxide Reductase (AhpC) Have Compensatory Roles in Peroxide Stress Resistance and Are Required for Survival, Persistence, and Nasal Colonization in *Staphylococcus aureus*. *J Bacteriol*. 2007; 189:1025–1035. [PubMed: 17114262]
- Baker LMS, Raudonikiene A, Hoffman PS, Poole LB. Essential Thioredoxin-Dependent Peroxiredoxin System from *Helicobacter pylori*: Genetic and Kinetic Characterization. *J Bacteriol*. 2001; 183:1961–1973. [PubMed: 11222594]
- Mehta NS, Benoit SL, Mysore J, Maier RJ. In vitro and in vivo characterization of alkyl hydroperoxide reductase mutant strains of *Helicobacter hepaticus*. *Biochim Biophys Acta*. 2007; 1770:257–265. [PubMed: 17098365]
- Wood ZA, Poole LB, Karplus PA. Peroxiredoxin Evolution and the Regulation of Hydrogen Peroxide Signaling. *Science*. 2003; 300:650–653. [PubMed: 12714747]
- Rhee SG, Woo HA, Kil IS, Bae SH. Peroxiredoxin Functions as a Peroxidase and a Regulator and Sensor of Local Peroxides. *J Biol Chem*. 2012; 287:4403–4410. [PubMed: 22147704]
- Giorgio M, Trinei M, Migliaccio E, Pelicci PG. Hydrogen peroxide: a metabolic byproduct or a common mediator of ageing signals? *Nat Rev Mol Cell Biol*. 2007; 8:722–728. [PubMed: 17700625]
- Rhee SG, Yang KS, Kang SW, Woo HA, Chang TS. Controlled Elimination of Intracellular H<sub>2</sub>O<sub>2</sub>: Regulation of Peroxiredoxin, Catalase, and Glutathione Peroxidase via Post-translational Modification. *Antiox & Redox Signaling*. 2005; 7:619–626.
- Haque A, Andersen JN, Salmeen A, Barford D, Tonks NK. Conformation-Sensing Antibodies Stabilize the Oxidized Form of PTP1B and Inhibit Its Phosphatase Activity. *Cell*. 2011; 147:185–198. [PubMed: 21962515]

15. Kil IS, et al. Feedback Control of Adrenal Steroidogenesis via H<sub>2</sub>O<sub>2</sub>-Dependent, Reversible Inactivation of Peroxiredoxin III in Mitochondria. *Mol Cell*. 2012; 46:584–594. [PubMed: 22681886]
16. Zykova TA, et al. T-LAK Cell-originated Protein Kinase (TOPK) Phosphorylation of PrxI at Ser-32 Prevents UVB-induced Apoptosis in RPMI7951 Melanoma Cells through the Regulation of PrxI Peroxidase Activity. *J Biol Chem*. 2010; 285:29138–29146. [PubMed: 20647304]
17. Chang TS, Jeong W, Choi SY, Yu S, Kang SW, Rhee SG. Regulation of Peroxiredoxin I Activity by Cdc2-mediated Phosphorylation. *J Biol Chem*. 2002; 277:25370–25376. [PubMed: 11986303]
18. Parmigiani RB, Xu WS, Venta-Perez G, Erdjument-Bromage H, Yaneva M, Tempst P, Marks PA. HDAC6 is a specific deacetylase of peroxiredoxins and is involved in redox regulation. *PNAS*. 2008; 105:9633–9638. [PubMed: 18606987]
19. Park JW, Piszczek G, Rhee SG, Chock PB. Glutathionylation of Peroxiredoxin I Induces Decamer to Dimers Dissociation with Concomitant Loss of Chaperone Activity. *Biochemistry*. 2011; 50:3204–3210. [PubMed: 21401077]
20. Schröder E, Willis AC, Ponting CP. Porcine natural-killer-enhancing factor-B: oligomerisation and identification as a calpain substrate in vitro. *Biochim Biophys Acta*. 1998; 1383:279–291. [PubMed: 9602152]
21. Nelson KJ, Knutson ST, Soito L, Klomsiri C, Poole LB, Fetrow JS. Analysis of the peroxiredoxin family: Using active-site structure and sequence information for global classification and residue analysis. *Proteins: Struct Funct Bioinform*. 2010; 79:947–964.
22. Wood ZA, Poole LB, Hantgan RR, Karplus PA. Dimers to doughnuts: redox-sensitive oligomerization of 2-cysteine peroxiredoxins. *Biochemistry*. 2002; 41:5493–5504. [PubMed: 11969410]
23. Nelson KJ, Parsonage D, Hall A, Karplus PA, Poole LB. Cysteine pKa Values for the Bacterial Peroxiredoxin AhpC. *Biochemistry*. 2008; 47:12860–12868. [PubMed: 18986167]
24. Hall A, Parsonage D, Poole LB, Karplus PA. Structural Evidence that Peroxiredoxin Catalytic Power Is Based on Transition-State Stabilization. *J Mol Biol*. 2010; 402:194–209. [PubMed: 20643143]
25. Perkins A, Gretes MC, Nelson KJ, Poole LB, Karplus PA. Mapping the Active Site Helix-to-Strand Conversion of CxxxxC Peroxiredoxin Q Enzymes. *Biochemistry*. 2012; 51:7638–7650. [PubMed: 22928725]
26. Ådén J, et al. Extraordinary μs–ms backbone dynamics in *Arabidopsis thaliana* peroxiredoxin Q. *Biochim Biophys Acta (BBA) - Proteins and Proteomics*. 2011; 1814:1880–1890.
27. Cao Z, Tavender TJ, Roszak AW, Cogdell RJ, Bulleid NJ. Crystal structure of reduced and of oxidized peroxiredoxin IV enzyme reveals a stable oxidized decamer and a non-disulfide-bonded intermediate in the catalytic cycle. *J Biol Chem*. 2011; 286:42257–42266. [PubMed: 21994946]
28. Parsonage D, Karplus PA, Poole LB. Substrate specificity and redox potential of AhpC, a bacterial peroxiredoxin. *PNAS*. 2008; 105:8209–8214. [PubMed: 18165315]
29. Parsonage D, Youngblood DS, Sarma GN, Wood ZA, Karplus PA, Poole LB. Analysis of the Link between Enzymatic Activity and Oligomeric State in AhpC, a Bacterial Peroxiredoxin. *Biochemistry*. 2005; 44:10583–10592. [PubMed: 16060667]
30. Baba T, et al. Construction of *Escherichia coli* K-12 in-frame, single-gene knockout mutants: the Keio collection. *Mol Syst Biol*. 2006; 2:2006.0008.
31. Studier FW. Protein production by auto-induction in high-density shaking cultures. *Protein Expression Purif*. 2005; 41:207–234.
32. Poole LB. Flavin-Dependent Alkyl Hydroperoxide Reductase from *Salmonella typhimurium*. 2. Cystine Disulfides Involved in Catalysis of Peroxide Reduction. *Biochemistry*. 1996; 35:65–75. [PubMed: 8555199]
33. Sarma GN, Nickel C, Rahlfs R, Fischer M, Becker K, Karplus PA. Crystal Structure of a Novel Plasmodium falciparum 1-Cys Peroxiredoxin. *J Mol Biol*. 2005; 346:1021–1034. [PubMed: 15701514]
34. Mizohata E, Sakai H, Fusatomi E, Terada T, Murayama K, Shirouzu M, Yokoyama S. Crystal structure of an archaeal peroxiredoxin from the aerobic hyperthermophilic crenarchaeon *Aeropyrum pernix* K1. *J Mol Biol*. 2005; 354:317–329. [PubMed: 16214169]

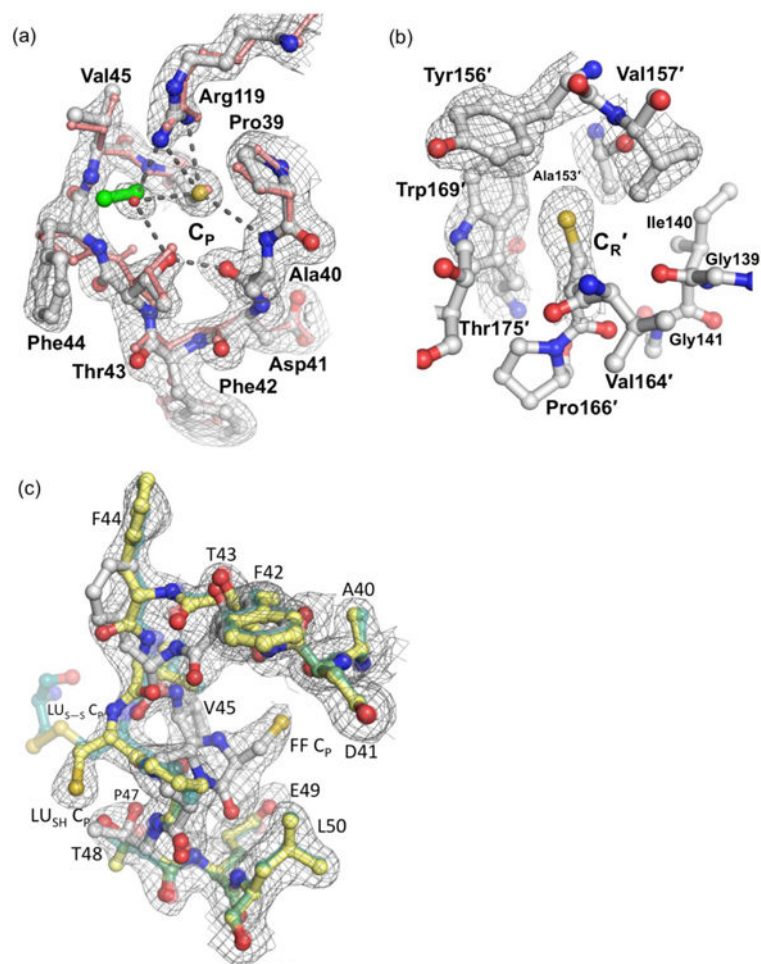
35. Battye TGG, Kontogiannis L, Johnson O, Powell HR, Leslie AGW. iMOSFLM: a new graphical interface for diffraction-image processing with MOSFLM. *Acta Crystallogr Sect D: Biol Crystallogr.* 2011; 67:271–281. [PubMed: 21460445]
36. Karplus PA, Diederichs K. Linking Crystallographic Model and Data Quality. *Science.* 2012; 336:1030–1033. [PubMed: 22628654]
37. Driggers CM, Cooley RB, Sankaran B, Hirschberger LL, Stipanuk MH, Karplus PA. Cysteine Dioxygenase Structures from pH 4 to 9: Consistent Cys-Persulfenate Formation at Intermediate pH and a Cys-Bound Enzyme at Higher pH. *J Mol Biol.* 2013; 425:3121–3136. [PubMed: 23747973]
38. Evans PR, Murshudov GN. How good are my data and what is the resolution? *Acta Crystallogr Sect D: Biol Crystallogr.* 2013; 69:1204–1214. [PubMed: 23793146]
39. Smart OS, et al. Exploiting structure similarity in refinement: automated NCS and target-structure restraints in BUSTER. *Acta Crystallogr Sect D: Biol Crystallogr.* 2012; 68:368–380. [PubMed: 22505257]
40. Emsley P, Cowtan K. Coot: model-building tools for molecular graphics. *Acta Crystallogr Sect D: Biol Crystallogr.* 2004; 60:2126–2132. [PubMed: 15572765]
41. Afonine PV, et al. Towards automated crystallographic structure refinement with phenix.refine. *Acta Crystallogr Sect D: Biol Crystallogr.* 2012; 68:352–367. [PubMed: 22505256]
42. Rhoads TW, et al. Measuring copper and zinc superoxide dismutase from spinal cord tissue using electrospray mass spectrometry. *Anal Biochem.* 2011; 415:52–58. [PubMed: 21453670]
43. Rhoads TW, Williams JR, Lopez NI, Morré JT, Bradford CS, Beckman JS. Using Theoretical Protein Isotopic Distributions to Parse Small-Mass-Difference Post-Translational Modifications via Mass Spectrometry. *J Am Soc Mass Spectrom.* 2013; 24:115–124. [PubMed: 23247967]
44. Nelson KJ, Parsonage D, Karplus PA, Poole LB. Evaluating peroxiredoxin sensitivity toward inactivation by peroxide substrates. *Meth Enzymol.* 2013; 527:21–40. [PubMed: 23830624]
45. Kitano K, Niimura Y, Nishiyama Y, Miki K. Stimulation of Peroxidase Activity by Decamerization Related to Ionic Strength: AhpC Protein from *Amphibacillus xylanus*. *J Biochem.* 1999; 126:313–319. [PubMed: 10423523]
46. Matsumura T, et al. Dimer-Oligomer Interconversion of Wild-type and Mutant Rat 2-Cys Peroxiredoxin Disulfide Formation at Dimer-Dimer Interfaces is not Essential for Decamerization. *J Biol Chem.* 2008; 283:284–293. [PubMed: 17974571]
47. Smeets A, Loumaye E, Clippe A, Rees JF, Knoops B, Declercq JP. The crystal structure of the C45S mutant of annelid *Arenicola marina* peroxiredoxin 6 supports its assignment to the mechanistically typical 2-Cys subfamily without any formation of toroid-shaped decamers. *Protein Sci.* 2008; 17:700–710. [PubMed: 18359859]
48. Hall A, Sankaran B, Poole LB, Karplus PA. Structural Changes Common to Catalysis in the Tpx Peroxiredoxin Subfamily. *J Mol Biol.* 2009; 393:867–881. [PubMed: 19699750]
49. Stehr M, Hecht HJ, Jäger T, Flohé L, Singh M. Structure of the inactive variant C60S of *Mycobacterium tuberculosis* thiol peroxidase. *Acta Crystallogr Sect D: Biol Crystallogr.* 2006; 62:563–567. [PubMed: 16627951]
50. Choi J, et al. Crystal structure of the C107S/C112S mutant of yeast nuclear 2-Cys peroxiredoxin. *Proteins: Struct Funct Bioinform.* 2005; 61:1146–1149.
51. D'Ambrosio K, Limauro D, Pedone E, Galdi I, Pedone C, Bartolucci S, De Simone G. Insights into the catalytic mechanism of the Bcp family: Functional and structural analysis of Bcp1 from *Sulfolobus solfataricus*. *Proteins: Struct Funct Bioinform.* 2009; 76:995–1006.
52. Limauro D, D'Ambrosio K, Langella E, De Simone G, Galdi L, Pedone C, Pedone E, Bartolucci S. Exploring the catalytic mechanism of the first dimeric Bcp: Functional, structural and docking analyses of Bcp4 from *Sulfolobus solfataricus*. *Biochimie.* 2010; 92:1435–1444. [PubMed: 20637256]
53. Liao SJ, Yang CY, Chin KH, Wang AHJ, Chou SH. Insights into the Alkyl Peroxide Reduction Pathway of *Xanthomonas campestris* Bacterioferritin Comigratory Protein from the Trapped Intermediate-Ligand Complex Structures. *J Mol Biol.* 2009; 390:951–966. [PubMed: 19477183]

54. Melchers J, Diechtierow M, Feher K, Sinning I, Tews I, Krauth-Siegel RL, Muhle-Goll C. Structural Basis for a Distinct Catalytic Mechanism in *Trypanosoma brucei* Tryparedoxin Peroxidase. *J Biol Chem.* 2008; 283:30401–30411. [PubMed: 18684708]
55. Muhle-Goll C, Füller F, Ulrich AS, Krauth-Siegel RL. The conserved Cys76 plays a crucial role for the conformation of reduced glutathione peroxidase-type tryparedoxin peroxidase. *FEBS Lett.* 2010; 584:1027–1032. [PubMed: 20122932]
56. Nakamura T, Kado Y, Yamauchi T, Matsumara H, Ishikawa K, Inoue T. Crystal Structure of Peroxiredoxin from *Aeropyrum pernix* K1 Complexed with its Substrate, Hydrogen Peroxide. *J Biochem.* 2010; 147:109–115. [PubMed: 19819903]
57. Zhou P, Tian F, Lv F, Shang Z. Geometric characteristics of hydrogen bonds involving sulfur atoms in proteins. *Proteins: Struct Funct Bioinform.* 2009; 76:151–163.
58. Platts JA, Howard ST, Bracke BR. Directionality of Hydrogen Bonds to Sulfur and Oxygen. *J Am Chem Soc.* 1996; 118:2726–2733.
59. Baker EN, Hubbard RE. Hydrogen bonding in globular proteins. *Prog Bioph Mol Biol.* 1984; 44:97–179.
60. Nirudodhi S, Parsonage D, Karplus PA, Poole LB, Maier CS. Conformational studies of the robust 2-Cys peroxiredoxin *Salmonella typhimurium* AhpC by solution phase hydrogen/deuterium (H/D) exchange monitored by electrospray ionization mass spectrometry. *Intern J Mass Spectr.* 2011; 302:93–100.
61. González-Mondragón E, Zubillaga RA, Saavedra E, Chanez-Cardenas ME, Perez-Montfort R, Hernandez-Arana A. Conserved Cysteine 126 in Triosephosphate Isomerase Is Required Not for Enzymatic Activity but for Proper Folding and Stability. *Biochemistry.* 2004; 43:3255–3263. [PubMed: 15023076]
62. Sayed AA, Williams DL. Biochemical Characterization of 2-Cys Peroxiredoxins from *Schistosoma mansoni*. *J Biol Chem.* 2004; 279:26159–26166. [PubMed: 15075328]
63. Koo KH, et al. Regulation of Thioredoxin Peroxidase Activity by C-terminal Truncation. *Arch Biochem Biophys.* 2002; 397:312–318. [PubMed: 11795888]
64. Wang F, et al. Targeted Inhibition of Mutant IDH2 in Leukemia Cells Induces Cellular Differentiation. *Science.* 2013; 340:622–626. [PubMed: 23558173]
65. Rhee SG, Jeong W, Chang TS, Woo HA. Sulfiredoxin, the cysteine sulfinic acid reductase specific to 2-Cys peroxiredoxin: its discovery, mechanism of action, and biological significance. *Kidney International.* 2007; 72:S3–S8. [PubMed: 17653208]
66. Davis IW, Murray LW, Richardson JS, Richardson DC. MOLPROBITY: structure validation and all-atom contact analysis for nucleic acids and their complexes. *Nucleic Acids Research.* 2004; 32:W615–W619. [PubMed: 15215462]
67. Harding MM, Nowicki MW, Walkinshaw MD. Metals in protein structures: a review of their principal features. *Crystallography Reviews.* 2010; 16:247–302.
68. Vaguine AA, Richelle J, Wodak SJ. SFCHECK: a unified set of procedures for evaluating the quality of macromolecular structure-factor data and their agreement with the atomic model. *Acta Crystallogr Sect D: Biol Crystallogr.* 1999; 55:191–205. [PubMed: 10089410]

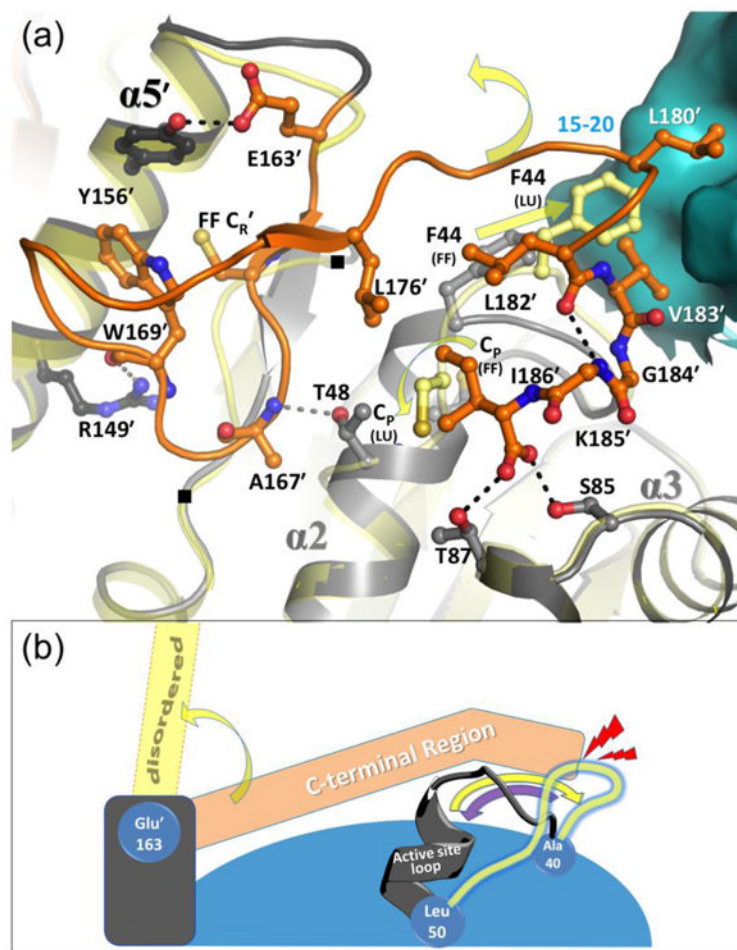




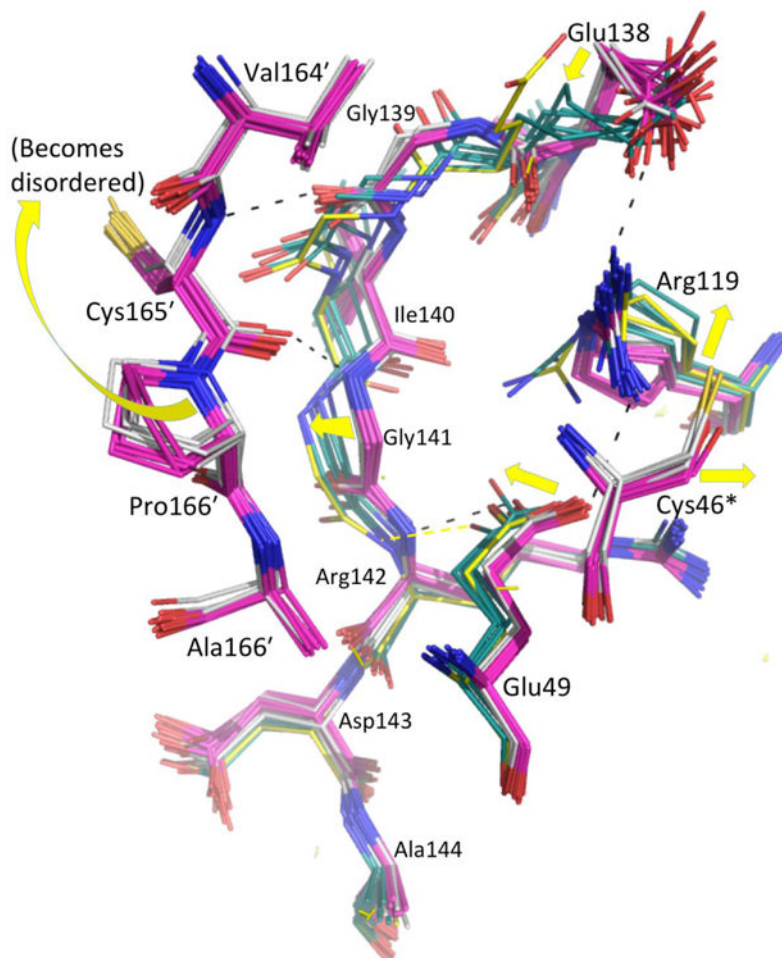




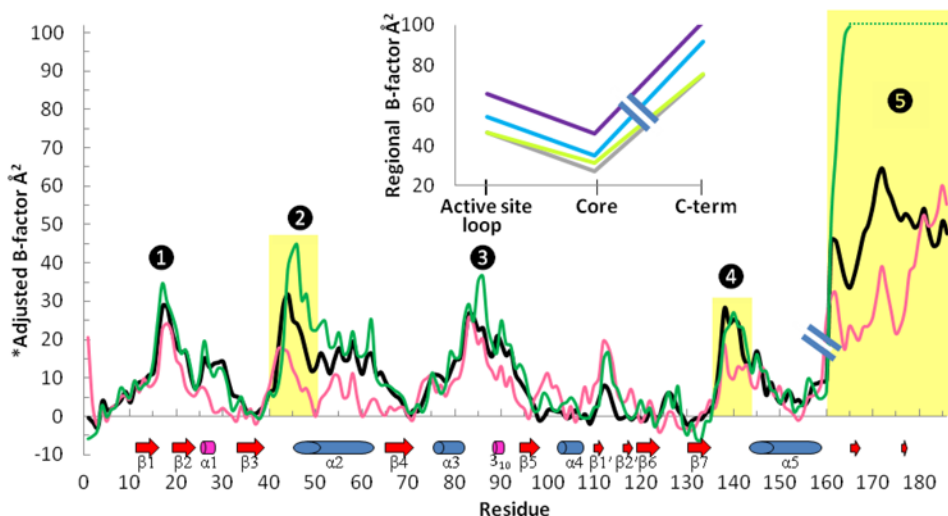
**Figure 3.** The WT<sub>DTT</sub> C<sub>P</sub> and C<sub>R</sub> environments in FF chains. (a) The FF active site loop of wild type *StAhpC* chain A (white) in 2F<sub>O</sub>-F<sub>C</sub> electron density (grey mesh contoured at 1.5  $\rho_{rms}$ ) matches the conformation of peroxide-bound *ApTpx* (pink protein and green peroxide; PDB code 3a2v). Selected polar interactions are indicated by dashed lines. In *StAhpC*, a bound water (red sphere) overlays with the position of the *ApTpx* hydrogen peroxide substrate. (b) The FF C<sub>R</sub> environment in chain B (white) is shown with 2F<sub>O</sub>-F<sub>C</sub> electron density (contoured at 1.0  $\rho_{rms}$ ). The FF C<sub>R</sub> is buried in a pocket formed by Ile140, Tyr156', Val157', Trp169', and Thr175' where it is sheltered from reacting with cellular oxidants and electrophiles. (c) The active site loop of chain B shown adopting both the FF path (solid white) and the LU<sub>SH</sub> path (solid yellow) with similar levels of 2F<sub>O</sub>-F<sub>C</sub> electron density (countered at 1.0  $\rho_{rms}$ ). The LU<sub>SH</sub> conformation is similar to that of LU<sub>S-S</sub> (transparent forest green; PDB code 1yep), but the C<sub>P</sub> thiol adopts a different position.



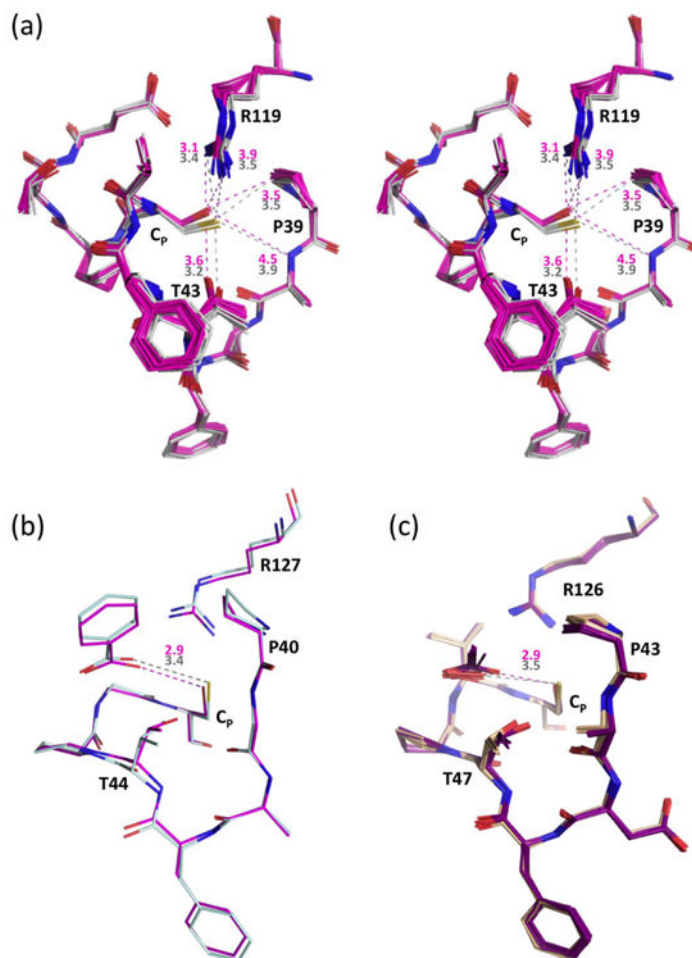
**Figure 4.** Packing interactions and coordination of unfolding of the FF C-terminal and active site loop regions. (a) The FF active site is shown (active site loop in grey; C-terminal region in dark orange; and the neighboring surface across the decamer-building interface in cyan) along with select interacting residues (labeled and shown as sticks) and stabilizing hydrogen bonds (dashed lines). Positions of residues 137 and 141 are also noted with (■). To provide context, the LU<sub>SH</sub> conformation (transparent yellow) is shown and yellow arrows indicate movements of the C<sub>P</sub> residue and Phe44. The C-terminal region has minimal regular secondary structure (residues Val164'–Cys165' forms a short  $\beta$ -strand and Leu180'–Gly184' is a short  $3_{10}$ -helix), and it interacts with helix  $\alpha 5'$  of the same chain (two H-bonds shown), across the decamer-building interface, and with the FF active site loop. The C-terminal residue Ile186' side chain packs with Pro47, and C-terminal  $\alpha$ -carboxylate H-bonds with the side chains of Ser85 and Thr87. (b) Cartoon scheme emphasizing that C-terminal region unfolding destabilizes but does not disrupt the active site loop, whereas active site loop unfolding does disrupt the folding of the C-terminal region. As in panel (a), FF conformations of the two regions are shown in grey and orange, yellow arrows indicate transitions to LU, and LU positions are depicted in transparent yellow. Shown also are approximate hinge points at Ala40, Leu50, and Glu163' (blue cogs), and the collision of the LU active site loop with the FF C-terminal region (red lightning). The purple arrow emphasizes that the active site loop is not blocked from folding. The decamer-building interactions are not shown in this scheme.



**Figure 5.** Role of the 137-142 segment in the FF $\leftrightarrow$ LU transition. Twenty-four FF dimers (C46S, pink; wild type, white) and 6 LU dimers (LU<sub>S-S</sub>, forest green; LU<sub>S-H</sub>, yellow) are shown, with yellow arrows highlighting FF $\rightarrow$ LU shifts. For clarity, only the FF position of C<sub>P</sub> (C46 or S46, denoted with an asterisk) is shown. Select H-bonds shown link residues 139-141 in a  $\beta$ -sheet with the FF C-terminal region and via the Glu138 and Glu49 side chains, to the catalytic Arg119.

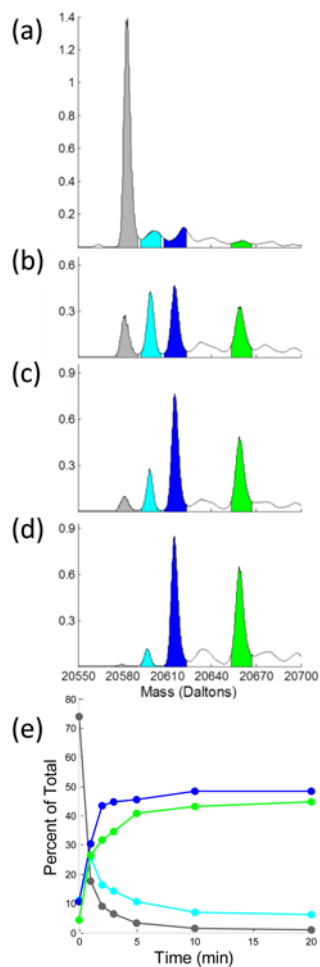


**Figure 6.** Mobility patterns in wild type *StAhpC* and  $C_P \rightarrow$  Ser structures. A hybrid plot of average main chain B-factors by residue is shown, with each color trace representing the B-factors for residues 1-160 of one chain and residues 161-186 of its dimer partner chain. Shown are the wild type FF AB' dimer (black), the  $LU_{S-S}$  AB' dimer (PDB code 1yep; forest green), and a dimer from FF C46S with a solvent exposed active site (PDB code 1n8j KL' dimer; pink). To normalize comparisons, the B-factors were adjusted by subtracting a trace-specific “core” B-value (defined as the 10<sup>th</sup> percentile B-factor of atoms in the chain contributing residues 1-160). Indicated below the plot are the positions of secondary structures (labeled). The peaks labeled 1 to 5 are the segments involved in the FF $\leftrightarrow$ LU transition, with regions that move highlighted in gold. In C46S, the less-ordered N-terminus may be due to the lack of a chloride ion in this crystal form, and the low B-factors near residue 30 are due to a crystal packing interaction. Differences in the 100-130 region may be attributed to the unidentified ligand at the decamer-building interface (see Experimental Procedures, Fig. S3). Inset: Plotted are the average main chain B-factor for residues 40-50 (active site loop) and for residues 161'-186' (C-term), along with the 10<sup>th</sup> percentile B-value of the active site loop containing chain (Core) for each of the four FF<sub>WT</sub> active sites: AB' (grey), CD' (lime green), DC' (blue), and EE'<sub>sym</sub> (purple). The variation in absolute mobility among the four FF<sub>WT</sub> active sites relates to the crystal packing interactions, with for example, the EE'<sub>sym</sub> active site being the most disordered, because it has no crystal contacts (see also Fig. 1b).



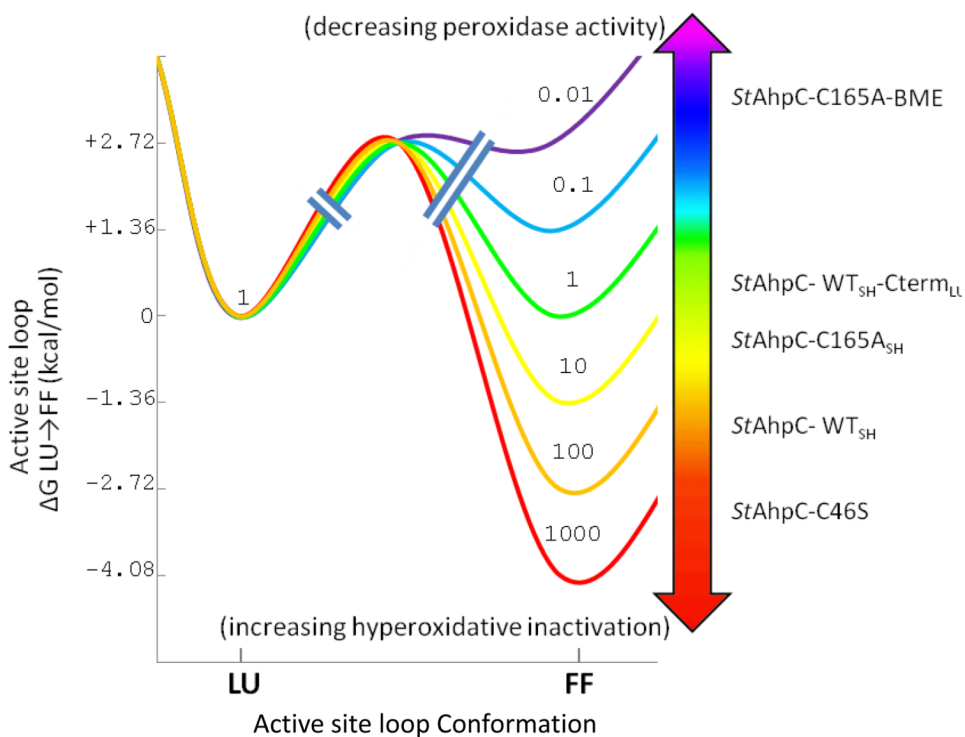
**Figure 7.**

Active site changes due to  $C_p \rightarrow Ser$  mutations. (a) Stereo diagram of 20 chains of C46S (pink) overlaid onto the 4 chains of wild type *StAhpC* (solid white), with representative distances given in Å based on C46S Chain K (pink) and wild type Chain A (grey). Estimation of coordinate uncertainty by SFCHECK<sup>68</sup> for both of these models are in the range of 0.2-0.3 Å. (b) Active site overlay of wild type *HsPrxV* (light blue, PDB code 1hd2) and its  $C_p \rightarrow Ser$  mutant (pink, PDB code 1urm) with color-coded distances to the bound benzoate indicated, which were chosen for comparison based on having resolution better than 2.0 Å, clear density for the ligands, and adoption of the same space group with similar unit cells. For 12 chains of wild type *HsPrxV* with benzoate, acetate, or DTT ligands (PDB codes 1hd2, 3mng, 1h4o, 1oc3, 2vl2, and 2vl3) the average Cys  $S\gamma \cdots$ ligand distance is 3.46 Å (c) Active site overlay of 10 chains from wild type *ApTpx* (light pink, peroxide-bound; PDB code 3a2v) and 10 chains from its  $C_p \rightarrow Ser$  mutant (purple, acetate bound; PDB code 3a2x) with the color-coded average distances indicated.



**Figure 8.**

Modifications of C165A *StAhpC* by 1 mM hydrogen peroxide. (a-d) Mass spectra of purified C165A *StAhpC* starting material and after treatment with 1 mM peroxide for 1, 3, and 20 min, respectively (see Experimental Procedures). The theoretical weight of C165A is 20584.32 Da ( $C_{928}H_{1427}N_{241}O_{283}S_3$ ), and for modifications: 20600.32 Da (+1 Oxygen) 20616.32 Da (+2 Oxygens), 20660.44 Da (BME adduct, +  $C_2H_4OS$ ). Experimental peaks have values of 20584 Da (grey), 20599 Da (cyan), 20615 Da (blue), and 20659 Da (green). Inferred identities of the observed species assume that additions are associated with the  $C_P$  residue. The y-axes are normalized so that the summed areas of the four colored peaks is a constant. (e) Integrated normalized populations of four prominent species as a function of time. We suspect that the time=0 populations attributed to SOH (cyan) and  $SO_2^-$  (blue) are overestimates, because the peak centers are not at the expected mass and they may be satellite peaks caused by some non-covalent ligand binding to the fully reduced protein. Fortunately, these areas are small and their inclusion does not substantially impact the conclusions.



**Figure 9.**

A thermodynamic framework for understanding the impact of Prx modifications on its function via alteration of the active site loop FF↔LU equilibrium. Plotted is an illustrative series of six possible free energy changes associated with the LU to FF transition with each 1.36 kcal/mol increment in their relative stabilities corresponding to a 10-fold change in the FF/LU equilibrium ratio at 298 K. The transition state barrier is not to scale, but for simplicity, we have drawn it as relatively low, consistent with the rapid dynamics seen for some Prxs.<sup>26</sup> Based on the relative strength of density observed for the FF and LU conformations in various crystal forms and active sites, we have roughly assigned the structures discussed here to the different curves. Along this series, *StAhpC* forms discussed in the text are shown at the point where we approximate their FF↔LU equilibria. As illustrated by the arrows, modifications that destabilize the FF active site will lower the initial rate of reaction with peroxides while protecting against hyperoxidation, whereas modifications that stabilize the FF will slow disulfide formation and increase the enzyme's susceptibility to hyperoxidation. These effects could, in theory, also be induced by inhibitors that stabilized either the LU or FF conformation.

**Table 1**  
**Data collection and refinement statistics**

<i>Data Collection</i>	<b>PDB code:4MA9</b>	<b>PDB code: 4MAB</b>
Structure	WT <sub>DTT</sub>	C165A <sub>DTT</sub>
Space group	C222 <sub>1</sub>	C222 <sub>1</sub>
Unit cell <i>a</i> , <i>b</i> , <i>c</i> (Å)	126.81, 171.13, 135.34	127.23, 172.42, 136.21
Resolution (Å)	36.8-1.82 (1.92-1.82) <sup>a</sup>	29.2-1.90 (2.00-1.90)
Completeness (%)	96.7 (91.1)	100.0 (100.0)
Unique reflections	126642 (17246)	117456 (17015)
Multiplicity	13.0 (12.7)	6.8 (6.4)
R <sub>meas</sub> (%)	23.1 <sup>b</sup> (408)	23.8 <sup>c</sup> (1048)
<I/σ>	10.6 (0.6) <sup>d</sup>	6.2 (0.2) <sup>e</sup>
CC <sub>1/2</sub>	1.00 (0.16)	0.995 (0.20)
<i>Refinement</i>		
Resolution range (Å)	36.7-1.82	29.2-1.90
R-factor (%)	20.4	19.8
R-free (%)	24.0	23.9
Molecules in AU	5	5
Protein residues	907	909
Water molecules	518	232
Total atoms	14776	14454
RMSD lengths (Å)	0.012	0.016
RMSD angles (°)	1.3	1.6
Ramachandran plot <sup>f</sup>		
φ, ψ-Preferred (%)	97.6	97.2
φ, ψ-Allowed (%)	2.4	2.7
φ, ψ-Outliers (%)	0.0	0.1 <sup>g</sup>
B factors		
	1 TLS group/monomer	1 TLS group/monomer
<Main chain> (Å <sup>2</sup> )	48	56
<Side chains & waters> (Å <sup>2</sup> )	59	64

<sup>a</sup>Values in parentheses are for the highest resolution shell and preceding values are for all data.

<sup>b</sup>R<sub>meas</sub> in the inner shell (40-5.76 Å) is 3.3%.

<sup>c</sup>R<sub>meas</sub> in the inner shell (30-6.01 Å) is 3.8%.

<sup>d</sup><I/σ> of the inner shell is 58.1 and falls to ~2 at 2.15 Å.

<sup>e</sup><I/σ> of the inner shell is 30.8 and falls to ~2 at 2.30 Å.


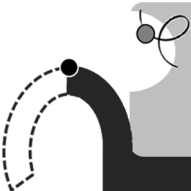

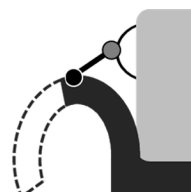
<sup>f</sup>Preferred, allowed, and outlier angles as assigned by Molprobity.<sup>66</sup>

<sup>g</sup>V164 chain A has weak density but is near an allowed region.



**Table 2**

Conformations and their occupancies as seen in representative active sites of *StAhpC* structures.<sup>a</sup>

	FF	LU <sub>C-term</sub>	LU <sub>SH</sub>	LU <sub>s,s</sub>
<b>Crystal: active sites</b>				
<b>WT<sub>brt</sub>: AB', CD', DC', EE'</b>	100	0	0	0
<b>WT<sub>brt</sub>: BA'</b>	0	50	50	0
<b>C165<sub>A<sub>brt</sub></sub>: AB', CD', DC', EE'</b>	60	20	20	0
<b>C165<sub>A<sub>brt</sub></sub>: BA'</b>	0	50	50	0
<b>C46S: all 20</b>	100	0	0	0
<b>WT<sub>s,s</sub>: all 5</b>	0	0	0	100

<sup>a</sup>The conformation names used are all described in the text and the cartoon images provide a simple visual of the essential features of the conformation with the CP shown as a grey circle and CR as a black circle. The four crystal forms listed are also described in the text.